BG Tri: an example of a low-inclination RW Sex-type nova-like

M. S. Hernández [1]★ G. Tovmassian,[2] S. Zharikov [2,3] B. T. Gänsicke,[4,5] D. Steeghs,[6,7]
A. Aungwerojwit[8] and P. Rodríguez-Gil[9,10]

[1]*Instituto de Física y Astronomía, Facultad de Ciencias, Universidad de Valparaíso, Av. Gran Bretaña, 1111 Valparaíso, Chile*
[2]*Instituto de Astronomía,Universidad Nacional Autónoma de México, Instituto de Astronomía, AP 106, Ensenada 22860, BC, Mexico*
[3]*Al-Farabi Kazakh National University, Al-Farabi Ave., 71, 050040 Almaty, Kazakhstan*
[4]*University of Warwick, Department of Physics, Gibbet Hill Road, Coventry CV4 7AL, UK*
[5]*Centre for Exoplanets and Habitability, University of Warwick, Coventry CV4 7AL, UK*
[6]*Department of Physics, Astronomy and Astrophysics Group, University of Warwick, Coventry CV4 7AL, UK*
[7]*Harvard-Smithsonian Center for Astrophysics, 60 Garden Street, Cambridge, MA 02138, USA*
[8]*Department of Physics, Faculty of Science, Naresuan University, Phitsanulok 65000, Thailand*
[9]*Instituto de Astrofísica de Canarias, Vía Láctea s/n, E-38205 La Laguna, Tenerife, Spain*
[10]*Departamento de Astrofísica, Universidad de La Laguna, E-38206 La Laguna, Tenerife, Spain*

ABSTRACT

We analyse a wealth of optical spectroscopic and photometric observations of the bright ($V = 11.9$) cataclysmic variable BG Tri. The *Gaia* DR2 parallax gives a distance $d = 334(8)$ pc to the source, making the object one of the intrinsically brightest nova-like variables seen under a low orbital inclination angle. Time-resolved spectroscopic observations revealed an orbital period of $P_{orb} = 3.8028(24)$ h. Its spectroscopic characteristics resemble RW Sex and similar nova-like variables. We disentangled the Hα emission line into two components, and show that one component forms on the irradiated face of the secondary star. We suggest that the other one originates at a disc outflow area adjacent to the L3 point.

Key words: cataclysmic variables – dwarf novae – white dwarf – stars: individual: BG Tri.

1 INTRODUCTION

Cataclysmic variables (CVs) are close binary systems comprising a white dwarf (WD) and a low-mass star losing matter in a Roche lobe overflow regime, usually creating an accretion disc around the accreting WD (Warner 1995). CVs show diverse observational characteristics depending on their fundamental physical properties, including orbital period, mass- ransfer rate, and the strength of the magnetic field of the WD. Their diversity is also in part due to the viewing angle (Howell & Mason 2018). In non- or weakly magnetic systems, the accretion flow takes place in a fully developed accretion disc. At high mass-transfer rates ($\geq 10^{-9}$ M$_\odot$ yr^{-1}), these are hot steady-state discs (Baptista, Steiner & Horne 1996). Therefore, the disc thermal instability that triggers dwarf nova outbursts is prevented (Shafter, Wheeler & Cannizzo 1986; Shafter 1992; Lasota 2001). These high mass-transfer rate systems are known as nova-like variables (NLs), because it was initially argued that they might potentially exhibit or have undergone undetected nova eruptions (Vorontsov-Velyaminov 1934). No known NL has ever been seen to erupt as a nova. However, some NLs may resemble novae when the nova returns to a quiescent state after the eruption (Warner 1995). They constitute a small fraction of the entire CV population (∼15 per cent in Ritter & Kolb 2003a, b), which might be the result of an observational bias. The vast majority of NLs have orbital periods above the so-called 'period gap' (Rappaport, Verbunt & Joss 1983; Kolb, King & Ritter 1998; Zorotovic et al. 2016; Abril et al. 2020).

We exclude CVs with moderately or highly magnetic WDs, which historically were also accounted for as NLs.

There is a visible differentiation between NLs and dwarf novae in terms of their orbital periods and colours (Abril et al. 2020). It is noticeable that NLs dominate the orbital period range 3–4 h, where very few dwarf novae are observed (Knigge, Baraffe & Patterson 2011). However, in absolute numbers, the amount and distribution of NLs and dwarf novae right above the period gap are comparable (Knigge et al. 2011). There is no good understanding why the two populations of NL and dwarf novae overlap in some period ranges but not in others. NLs have accretion rates that are higher than 'normal' CVs both at longer and shorter periods. They are intrinsically very bright, and their WDs tend to be hotter (Townsley & Gänsicke 2009).

The spectra of some NL variables display persistent broad Balmer absorption lines, indicative of optically thick discs. However, NLs themselves come in different flavours. A fraction of NLs, known as VY Scl stars, show occasional states of low mass-transfer rates, i.e. they become significantly fainter for prolonged periods of time (months to years, Warner & van Citters 1974; Rodríguez-Gil et al. 2020). However, the physical cause of these low mass-transfer states is still uncertain (Livio & Pringle 1994; King & Cannizzo 1998; Schmidtobreick et al. 2018).

SW Sex stars form a class of NL variables with distinctive spectroscopic behaviour (Thorstensen et al. 1991). They mostly cluster in the 3–4 h orbital period range (Rodríguez-Gil et al. 2007b). Baptista et al. (1996), Dhillon, Smith & Marsh (2013), and Tovmassian et al. (2014) proposed an extended hotspot as the predominant source of emission lines from the optically and physically thick disc. However, such an interpretation is challenged by

★ E-mail: mercedes.hernandez@postgrado.uv.cl, gag@astro.unam.mx

Rodríguez-Gil et al. (2007, 2015). A search for non-eclipsing SW Sex in the 3–4 h period range revealed systems with two-component emission lines (Rodríguez-Gil, Schmidtobreick & Gänsicke 2007a), but it was inconclusive whether these are low-inclination SW Sex objects. Conversely, two-component emission lines recently have been observed in a couple of the UX UMa-type NLs (which are the primary concern of this paper). For example, Hernandez et al. (2017), based on high-resolution spectroscopy, demonstrated that NLs RW Sex and RXS J064434.5+334451 show at least two components in the profiles of the Balmer emission lines. The narrow component with a low radial-velocity amplitude originates from the irradiated surface of the secondary facing the disc. The wide component is formed in an extended low-velocity region on the outskirts of the opposite side of the accretion disc with respect to the collision point of the accretion stream and the disc. Recently, Subebekova et al. (2020) claimed that this property is observed in RW Tri. They compiled a current list of similar NLs with orbital periods ≥ 4 h. For at least four of them, the components of H α emission closely resemble those seen in RW Sex.

Other interpretations of line provenance (including absorption features frequently flanking emission lines) in such NL systems have been put forward. Notably, the disc overflow model by Hellier (1996) and disc-wind interpretations and models (e.g. Patterson et al. 1996; Murray & Chiang 1996) are worth mentioning.

BG Tri is a bright object reported by Woźniak et al. (2004), Khruslov (2008) to show an irregular low-amplitude variability and is tentatively identified as a CV, citing ROTSE1, TYC2, and *ROSAT* detections. Accordingly, the object is also catalogued as TYC 2298 01538 and 1RXS J014448.4+323320. Makarov (2017) confirms its NL identification based on a distance estimate by *Gaia*[1] (Gaia Collaboration et al. 2018) in combination with *Galaxy Evolution Explorer (GALEX)* UV magnitudes (Martin et al. 2003). However, BG Tri has not been studied in detail until now. We report the results of the spectroscopic study of the object against a backdrop of the long-term photometry collected by the Catalina Real-time Transient Survey and the All Sky Automated Surveys (ASAS).

2 OBSERVATIONS AND REDUCTION

We present an extensive set of multiwavelength observations of BG Tri obtained by us as well as a variety of data collected in surveys.

2.1 Photometry

The data from the Catalina Real-time Transient Survey (CRTS) (Drake et al. 2009) and the All-Sky Automated Survey for Supernovae (ASAS SN) (Shappee et al. 2014; Kochanek et al. 2017) were used to produce the light curve (Fig. 1) of the object. The data were obtained in the *V* and *g* bands. The difference between filters *g* and *V* is not significant and the average colour index was $g - V \approx 0.0$. Most of the time BG Tri is bright (≈ 12 mag, one of the brightest CVs in apparent magnitude) and nearly constant with non-regular small amplitude variability. The average magnitude in the time stretch HJD 2456524.01 to HJD 2457668.08 is $V = 11.91$, with a deviation of ≈ 0.06 mag. The light curve shows one occasion of a large flux drop (~ 2.5 mag), with a duration of 176 d. The initial descent from the average $V \approx 11.9$ to ≈ 13.6 mag lasts about 40 d at a rate of 0.04 mag d^{-1}. Following a stand-still at that magnitude that lasts one month, the brightness briefly falls further (on HJD 2458373),

---

[1]$d = 334.013 \pm 7.65$ pc according to the revised estimate (Bailer-Jones et al. 2018).
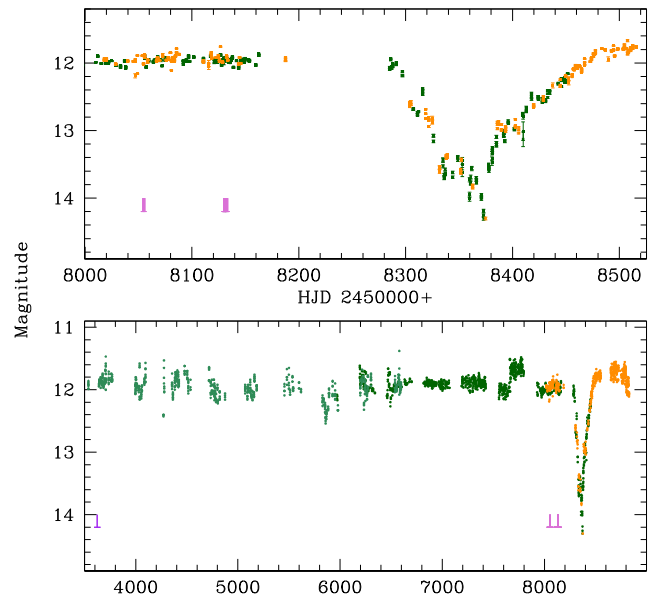
Figure 1. Long-term light curve of BG Tri obtained by the sky patrol ASAS SN and CRTS surveys. The dark green and orange points are ASAS data in *V* and *g* filters respectively, the light green points are CRTS *V*-band data. In the lower panel, the entire data set is presented, while the upper shows an expanded segment of the same during and around the low state. The magenta markers indicate moments of spectroscopic observations at the bottom of the light curve.

reaching $V = 14.3$ mag. From there, the luminosity starts to recover with a slower rate of 0.026 mag d^{-1}. This low-state episode, detailed in the upper panel of Fig. 1, is fairly common among NLs, classifying BG Tri as a VY Scl star. There is also an episode of a sudden jump of brightness detected between HJD 2457669.88 and HJD 2457797.72 before the antidwarf nova episode when the average brightness of the object reaches $V \approx 11.7$.

2.2 Spectroscopy

2.2.1 Low-resolution spectroscopy

A large number of low-resolution spectra were obtained with a variety of instruments listed in Table 1. At the 2.5-m Isaac Newton Telescope (INT), we used the intermediate dispersion spectrograph (IDS) with an R632V grating, the 2048 × 4100 pixel EEV10a CCD detector, and a 1.1 arcsec slit width. With this set-up, we sampled the wavelength region 4400–6700 Å at a full width at half maximum (FWHM) of ~ 2.5 Å resolution. More spectra were obtained using the blue arm of the intermediate dispersion spectrograph and imaging system (ISIS) mounted on the 4.2-m William Herschel Telescope at the Roque de los Muchachos Observatory on La Palma. Spectra of Cu–Ne–Ar comparison lamps were obtained every ~ 30–40 min in order to secure an accurate wavelength calibration.

Additional data were obtained with the Andalucía Faint Object Spectrograph and Camera (ALFOSC) at the 2.56-m Nordic Optical Telescope (NOT) on La Palma. The #8 CCD with a 2048 × 2048 pixel EEV chip was used for this observations. A spectral resolution of FHWM ∼ 3.7 Å was achieved by using grism #7 (plus the second-order blocking filter WG345) and a 1 arcsec slit width. The useful wavelength interval provided by this configuration is λλ 3800–6800. The spectroscopy at the 2.2-m Calar Alto (CA) telescope was performed with CAFOS. A 1.2 arcsec slit width and the G-100

Table 1. Log of spectroscopic observations.

Date	JD*	Range (Å)	No. of spectra	Exp. time (s)	Comments
2002 Aug 21	2507	3341–7546	2	200	INT
2002 Aug 23	2510	3341–7546	24	340	INT
2002 Aug 25	2512	3341–7546	15	120	INT
2002 Aug 31	2518	3341–7546	8	120	INT
2002 Sept 2	2520	3341–7546	4	120	INT
2002 Sept 3	2521	3341–7546	6	120	INT
2003 Oct 19	2932	3784–9063	2	60	ISIS B&R
2003 Dec 13	2987	4257–8318	4	120	CA
2003 Dec 14	2988	4257–8318	9	60	CA
2003 Dec 15	2989	4257–8318	2	60	CA
2003 Dec 16	2990	4257–8318	10	60	CA
2003 Dec 17	2991	4257–8318	10	60, 120	CA
2003 Dec 17	2991	3775–6840	7	120	NOT
2003 Dec 23	2997	4257–8318	6	60	CA
2003 Dec 24	2998	4257–8318	6	60	CA
2003 Dec 25	2999	4257–8318	2	60	CA
2003 Dec 26	3000	4257–8318	4	60	CA
2003 Dec 27	3001	4257–8318	2	60	CA
2004 Aug 9	3226	4257–8318	2	180	CA
2004 Aug 10	3227	4257–8318	2	180	CA
2004 Aug 11	3228	4257–8318	2	180	CA
2004 Aug 12	3229	4257–8318	2	180	CA
2004 Oct 21	3300	4257–8318	2	120	CA
2004 Oct 23	3302	4257–8318	2	120	CA
2004 Oct 24	3303	4257–8318	2	120	CA
2004 Oct 26	3305	4257–8318	2	120	CA
2004 Sept 10	3623	4257–8318	2	120	CA
2004 Nov 4	3314	3775–6840	2	120	NOT
2005 Jan 1	3372	3784–9063	2	200	ISIS B&R
2005 Jan 4	3375	3784–9063	2	200	ISIS B&R
2005 Jan 5	3376	3784–9063	2	200	ISIS B&R
2005 Jan 6	3377	3784–9063	2	200	ISIS B&R
2005 Jan 7	3378	3784–9063	2	200	ISIS B&R
2005 Sept 10	3623	4257–8318	2	120	CA
2017 Oct 27	8053	3600–7300	3	1200	Echelle
2017 Oct 28	8054	3600–7300	3	1200	Echelle
2017 Oct 29	8055	3600–7300	3	1200	Echelle
2018 Jan 11	8129	3600–7300	13	1200	Echelle
2018 Jan 12	8130	3600–7300	12	1200	Echelle
2018 Jan 13	8131	3600–7300	3	1200	Echelle
2018 Jan 14	8132	3600–7300	10	1200	Echelle

Note. *245 0000+ JD is given at beginning of the observing night. B&R: Blue and Red gratings.

grism granted access to the $\lambda\lambda$ 4200–8300 range with a resolution of FWHM $\sim$ 4.5 Å on the standard SITe CCD (2048 × 2048 pixels). After the effects of bias and flat-field structure were removed from the raw images, the sky background was subtracted. The one-dimensional target spectra were then obtained using the optimal extraction algorithm of Horne (1986). For wavelength calibration, a low-order polynomial was fitted to the arc data; the rms was always smaller than one-tenth of the dispersion in all cases. The pixel–wavelength correspondence for each target spectrum was obtained by interpolating between the two nearest arc spectra. The preliminary reduction steps for all low-resolution spectra were performed with the standard packages for long-slit spectra within IRAF,[2] while

[2]IRAF is distributed by the National Optical Astronomy Observatories, which are operated by the Association of Universities for Research in Astronomy, Inc., under cooperative agreement with the National Science Foundation.

wavelength calibration and most of the subsequent analyses made use of Tom Marsh's MOLLY[3] package.

No flux calibration is available for the low-resolution spectra; hence we present in Fig. 2 a normalized spectrum obtained by combining data at different epochs with different telescopes/instruments. The low-resolution spectra failed to reveal significant radial-velocity (RV) variation.

The overall spectral behaviour of BG Tri does not change significantly from epoch to epoch. The spectra indicate a steep blue continuum with Balmer lines showing emission features embedded in broader absorption lines. The higher members of the Balmer series appear to have more intense absorption, while towards the lowest numbers the emission component dominates. Helium lines are also present in the spectrum. The neutral helium lines have complex profiles, especially at He I λ4471. Also visible are He II and Ca II lines. The spectra are typical of NL variables with an optically thick disc and low inclination.

2.2.2 High-resolution spectroscopy

The high-resolution observations were obtained with the echelle REOSC spectrograph (Levine & Chakarabarty 1995) attached to the 2.1-m Telescope of the Observatorio Astronómico Nacional at San Pedro Mártir during several nights in 2017 and 2018. The CCD 2048 × 2048 detector was used to obtain a spectral resolution of $R \sim 18\,000$. All observations were carried out with the 300 l mm^{-1} cross-dispersor, which has a blaze angle at around 5500 Å. The spectral coverage was about 3600–7300 Å. The exposure time for each spectrum was 1200 s. A Th–Ar lamp was used for wavelength calibration. The spectra were reduced using the *echelle* package in IRAF. Standard procedures, including bias subtraction, cosmic ray removal, and wavelength calibration, were carried out. No flat-field correction and flux calibration were attempted; instead, the normalized spectra were used for measurements and visualization. A log of all spectroscopic observations is shown in Table 1.

3 THE PHENOMENOLOGY OF BG TRI

In a discovery note, Khruslov (2008) points out that BG Tri is a variable star, probably a CV. Presented here, the long-term light curve and spectra leave no doubt that the first assessment was correct. However, CVs comprising a WD and a late red or brown dwarf secondary star come in different flavours depending on their orbital periods (or separation), mass accretion rate, and strength of the magnetic field of the WD. Absence of nova or dwarf nova outbursts in a period of time over 5000 d indicates that this is an NL variable. Moreover, an antidwarf nova occurrence registered in the light curve is another characteristic of bright NLs, which occasionally undergo a fall in brightness by more than one magnitude (Warner 1995).

Low-resolution spectra confirm the CV identification of BG Tri, which exhibits a standard set of hydrogen and helium lines, with higher numbers of the Balmer series showing wide adsorptions with embedded relatively narrow emissions. In Fig. 2, an averaged and combined spectrum obtained at different epochs is plotted. All significant spectral features are marked. A combination of emission and absorption features of Balmer lines usually occurs either in dwarf novae near period minima where the WD becomes dominant, or in NLs with optically thick discs.

[3]MOLLY is available at Tom Marsh's web page: http://deneb.astro.warwick.ac.uk/phsaap/software/.
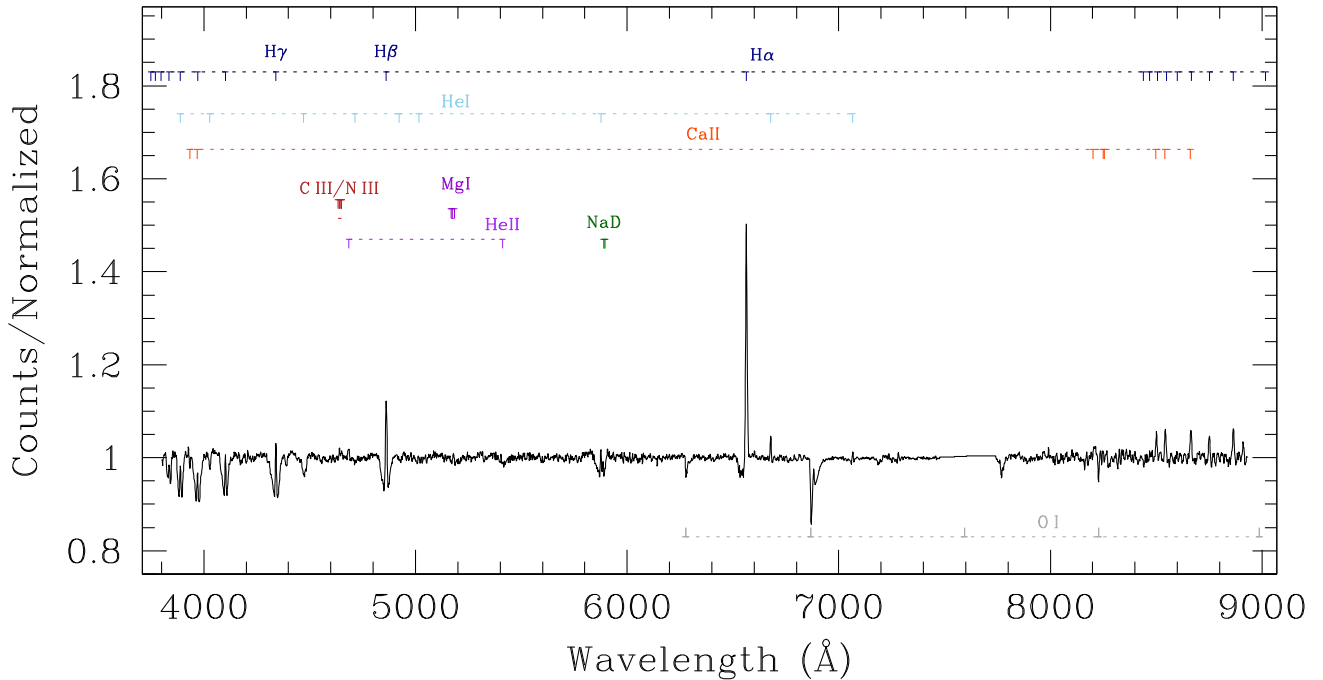
Figure 2. The combined and averaged low-resolution spectrum of BG Tri obtained at different epochs with different instruments. Major lines identified in the spectrum are marked on top, while atmospheric oxygen lines are marked at the bottom. The Mg I triplet is also marked, although we are not sure if it is real.

Using the *Gaia* distance $d = 334(8)$ pc to BG Tri, we calculate the absolute magnitude of the object $M_V = 4.26$. Such high luminosity puts BG Tri among the brightest CVs, only second after the infamous RW Sex (Hewitt et al. 2020). The derived absolute magnitude is consistent with the low inclination angle (Warner 1986, 1987). We will detail the spectral energy distribution (SED) and luminosity of the accretion disc later in the paper. Nevertheless, based only on the derived absolute magnitude, we can state that this object is not a low accretion rate WZ Sge type near the period minimum.

In NLs, the bulk of the accretion disc is optically thick (hot and dense), producing absorption lines. The emission lines are formed either in separate parts of the disc or by the gas in its vicinity (Warner 1976; Beuermann, Stasiewski & Schwope 1992). Fig. 3 displays a set of H I and He I line profiles from averaged and normalized high-resolution echelle spectra (with low-resolution profiles in the background), illustrating the composition of lines. In the averaged spectra, the emission profile of the Balmer lines is rather symmetric. The absorption is much wider and visually slightly blue-shifted with regard to the emission peak. Measuring this shift in spectra not corrected for instrumental sensitivity is complicated since the continuum is not well defined.

H α looks like it has a P Cyg profile with a blue-shifted absorption from a material rapidly expanding in the direction of the observer. However, this is just a contrast effect, particularly in the case of the low-resolution spectra. The emission feature is the strongest among the Balmer lines; hence the symmetry of the underlying absorption line is visually distorted. However, the composition of the line is similar to the rest of the Balmer lines; an emission peak is embedded in a wider absorption line. The helium lines show a more complicated structural comparison with the Balmer lines, as discussed below.

In general, BG Tri's spectrum looks like a replica of that of RW Sex (Hernandez et al. 2017) or IPHASX J210204.7+471015 (Guerrero et al. 2018). Hence, our approach to interpreting BG Tri builds on the assumption that it is a low-inclination NL system.

4 RADIAL VELOCITIES AND PERIOD DETERMINATION

Low-resolution spectra provided no information on the orbital motion of emission lines. This supports our assumption of a low orbital inclination. Hence, we obtained higher-resolution echelle spectra to reveal the orbital period of the object. Fitting H α emission with a single Gaussian produced a large scatter but no definite periodic pattern. However, measuring H β with a single Gaussian produced a time series that allowed us to determine a possible period and its closest one-day alias. The power spectrum calculated using a discrete Fourier transformation provided by Period 04 (Lenz & Breger 2014, 2005) indicated that the orbital frequency was either $\sim$5.3 cycles per day (c d^{-1}) or $\sim$6.3 c d^{-1} (see the bottom panel of Fig. 4). It was clear that the complications related to the period determination were due to lines that are composed of two or more components, as evident from the study of similar objects (Hernandez et al. 2017; Guerrero et al. 2018).

Now that we have an estimate of the orbital period, we further improve the obtained result by measuring the individual components of the lines. In the high-resolution spectra, the H α line is the strongest feature. It is also the least affected by the absorption accompanying all H emission lines. In general, it looks like a one-peak line, but with variable wings. We applied the line-deblending *splot* procedure in IRAF to separate the line into components. We fit the profile with two Gaussians with unrestricted parameters. The details of the method are provided in Tovmassian et al. (2018).

We seek a periodic sinusoidal pattern in the RV/time-space by eye and assign measurements of RVs to one or more component(s), in all cases when they are clearly distinct. Sometimes just one component stands out. We determine a more accurate orbital period by subjecting the first emerging periodic pattern to the Fourier analysis. Period 04 was used to determine the best choice of the orbital period. We refine RVs by fitting a sine-curve to the measurements of the better defined component and perform another round of deblending by
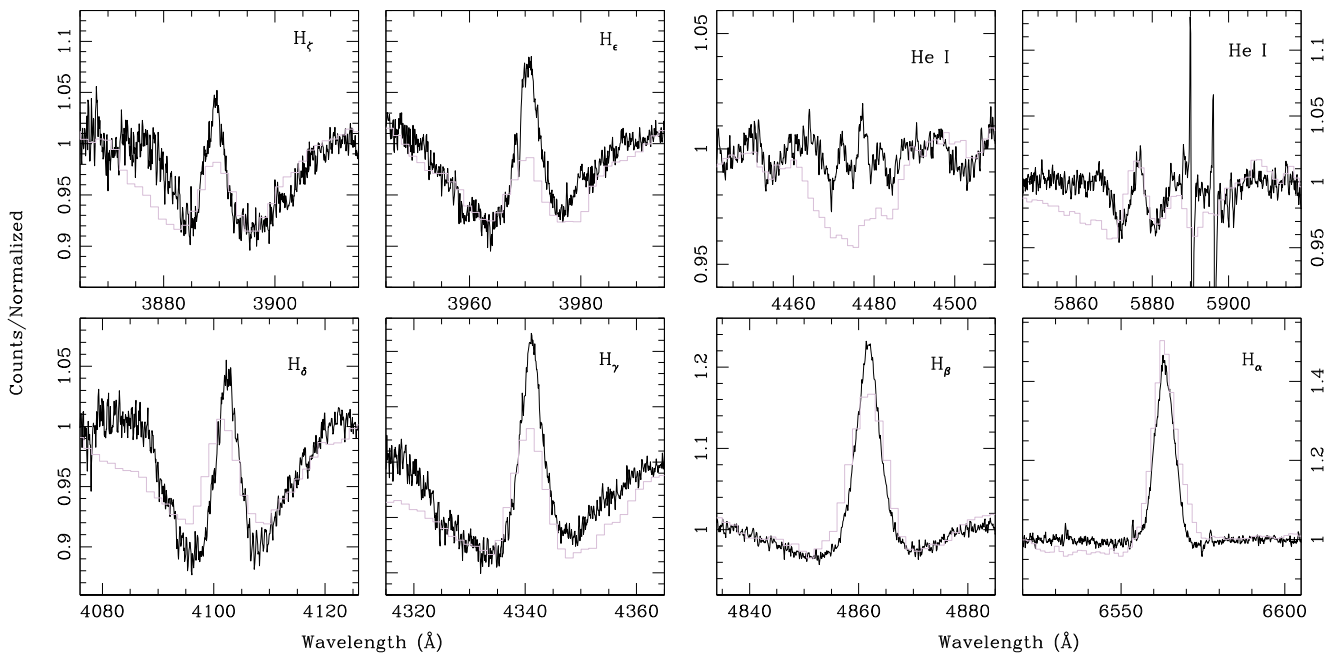
Figure 3. The profiles of important lines in the spectrum of BG Tri from the echelle spectra. The lines are marked in the upper corner of each panel. The black line is the median of all high-resolution spectra, while the low-resolution spectra from Fig. 2 are presented in the background.
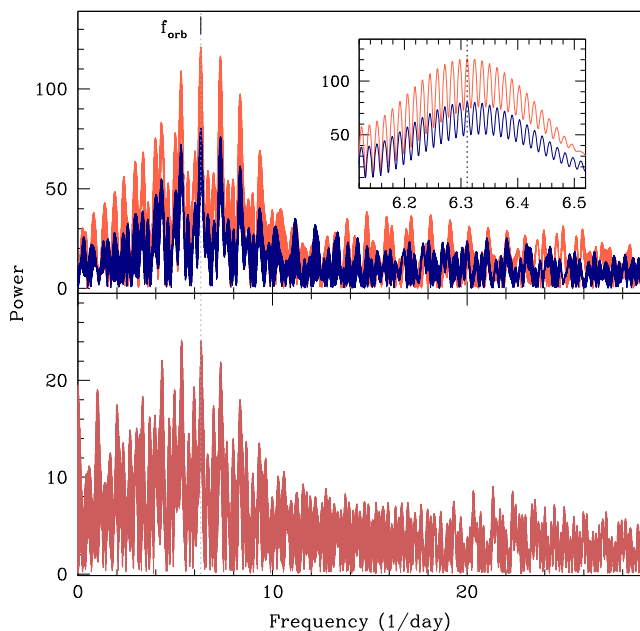

Figure 4. The power spectra of BG Tri calculated for the radial-velocity curves of different lines and components. In the upper panel the red and blue lines are the power of the HVC and the LVC after decomposition of the Hα line. In the inset an enlargement of the small range of frequencies around the derived period is presented. The bottom panel shows the power of Hβ measured with a single Gaussian.

fixing the central wavelength of this component. As a result, we improve the determination of the second component, which can be used to measure the orbital period. The difference in values of the orbital period from the two components is rather small. The higher-velocity amplitude component (HVC) power spectrum peaks at $6.311\,14\,c\,d^{-1}$, while the lower-velocity amplitude component

(LVC) has a frequency of $6.337\,94\,c\,d^{-1}$. The spread of measurements remains high. The residuals (rms) of the fit of the HVC are $36\,km\,s^{-1}$ with the amplitude of variation $121\,km\,s^{-1}$. The LVC has an amplitude of $78\,km\,s^{-1}$ and rms of $25\,km\,s^{-1}$. They reconcile better at the period determined from the HVC, which we adopted as the orbital period of $P_{orb} = 3.8028(24)\,h = 0.158\,45(10)\,d$. The power spectra obtained from the RVs of Hβ and two components of Hα are presented in Fig. 4. Obviously, the power of Hβ as a whole is much smaller than the power of separate components of Hα, but they are all consistent with one another.

The RV curves of the Hβ and Hα components along the measurements folded with the determined orbital period are presented in the two middle panels of Fig. 5, respectively. We assign phase zero to the negative-to-positive crossing of the LVC. Plots are flanked by trailed spectra of the corresponding lines on both sides. In the upper panel of Fig. 6 Gaussian profiles of individual components, their sum, and the observed line profiles in four different orbital phases are presented to illustrate the result of the separation of the line into two components. Residual spectra of individual components, as well as residuals after subtraction of both components, are displayed in the bottom panel. Hβ is probably also multicomponent, but dismantling it into components is rather difficult. There is a stronger absorption undermining the wings of the emission components. One component (the HVC) dominates, as is evident from Fig. 5. The amplitude of the fitted sine-curve to single-Gaussian measurements of the line is only $24\,km\,s^{-1}$, decreasing to $22\,km\,s^{-1}$ if the adopted $0.158\,45\,d$ period is used to fit the data. The rms is $16\,km\,s^{-1}$.

Armed with a set of two components comprising Hα, we may try to figure out their origin. We compare our spectroscopic observation with a small sample of similar objects published recently (Hernández Santisteban et al. 2017; Hernandez et al. 2017), which show similar two-component emission lines. RW Sex and 1RXS J064434.5+334451 (Hernandez et al. 2017) and RW Tri (Subebekova et al. 2020) were all observed with the same instrumental settings as BG Tri, so the measurements are uniform and the
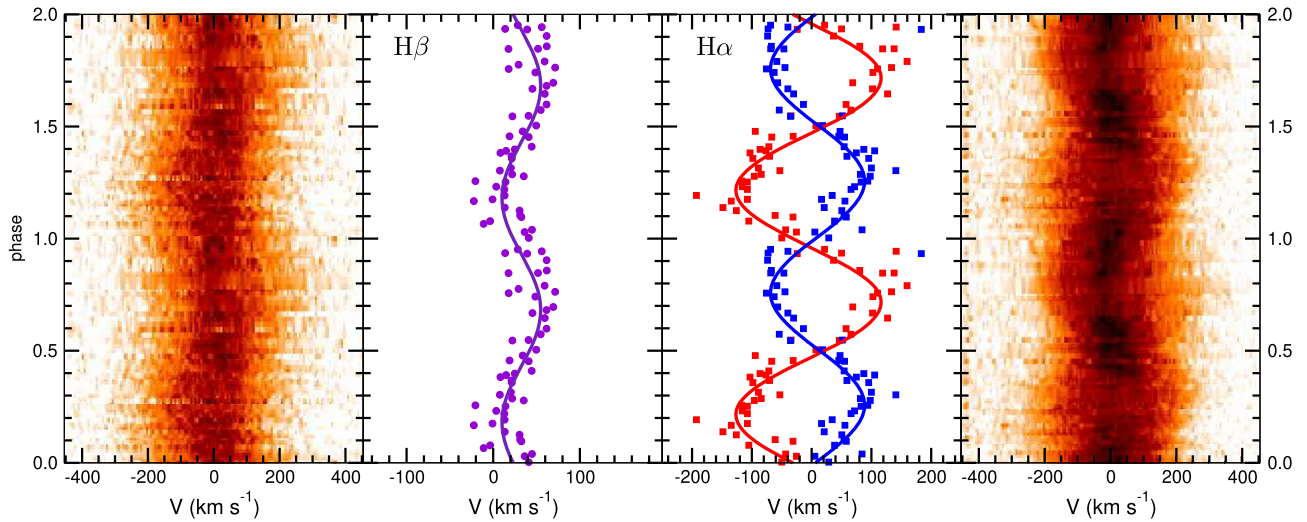
Figure 5. RV curves of Hβ and the components of Hα folded with the orbital period (left and right respectively). The RV of the Hβ line was first measured by fitting a single Gaussian, which enabled determination of the orbital period. Hα was separated into two components by fitting two Gaussians (see text for a description). The RV measurements corresponding to the high-velocity component of Hα are marked by red symbols and the fit to them with 121 km s^{-1} semi-amplitude as a red line. Respectively, the low-velocity component is plotted in blue. The semi-amplitude of the best-fitting curve is 74 km s^{-1}.
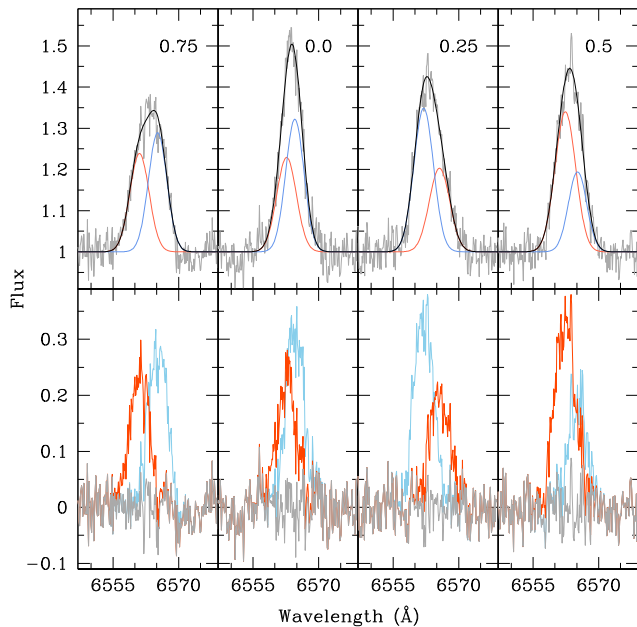
Figure 6. The line-profile phase evolution of Hα. Four orbital phases (marked in the upper right-hand corner of each panel) are displayed. In the upper panels the grey lines are the observed spectra. Two Gaussians obtained as a result of deblending are plotted by red and blue curves. Their sum is plotted by a black line as a fit to the observed profile. In the bottom panels the residuals of subtraction of the counterpart Gaussian are shown by red and blue lines, while the grey line is after subtraction of both Gaussians.

comparison is straightforward. All three objects show two distinct components varying with the respective orbital periods in almost counterphase relative to one another. One component is usually wider. Another, the narrow one, is firmly linked to the irradiated face of the secondary by two eclipsing objects in the sample, for which the zero phases are known precisely. The wide component is also regularly the higher-velocity component in other NLs. In the case of BG Tri, the difference in the widths of the components is

insignificant, but the HVC is still slightly broader than the LVC (average FWHM = 5.7(8) Å versus 5.3(4) Å, respectively).

Assuming that the secondary star emits the LVC, in analogy with the above-mentioned NLs (Hernandez et al. 2017; Subebekova et al. 2020), we determine the orbital phase zero ($\varphi = 0$) of the system as the moment when the RV of the LVC changes sign from negative to positive, i.e. when the secondary star is in the inferior conjunction. In this case, the ephemeris of BG Tri can be expressed as

$$\mathrm{HJD}_{\varphi=0} = 2458053.45490(60) + 0.15845(10)\,\mathrm{d} \times E. \qquad (1)$$

All phases used in this paper were calculated with this ephemeris.

4.1 Doppler tomography

A customary way to illustrate the emission line behaviour is via trailed spectra and Doppler tomography (Marsh & Horne 1988). It is worth mentioning that Doppler tomography works best if the emitting particles are in the orbital plane, and the inclination of the system's orbital plane is high (Marsh 2005). In order to construct trailed spectra and Doppler maps, we used the phase zero as defined above, stemming from the assumption that the LVC is the component originating from the irradiated face of the secondary. With this premise, the Doppler tomograms presented in Figs 7 and 8 were constructed (Spruit 1998). Echelle high-resolution spectra were used for this purpose. The Doppler map of the Hα line without separation into two components was calculated, but is not presented here because it is less informative. Tomograms of unaltered lines were presented by Hernandez et al. (2017); Guerrero et al. (2018). Instead, we split the Hα line into components, as demonstrated in the bottom panel of Fig. 6, and made a tomogram of each component separately.

In the bottom panels of Fig. 7 trailed spectra (and their reconstructed counterparts) of Hα's HVC and LVC are presented side by side. Together, they form the trailed spectra of Hα shown on the right-hand side of Fig. 5. Meanwhile, in the upper panels, the velocity maps resulting from the Doppler tomography are shown. Locations of stellar components are marked by '$\times$', the centre of the masses by '$+$'. The Roche lobe of the secondary star and the
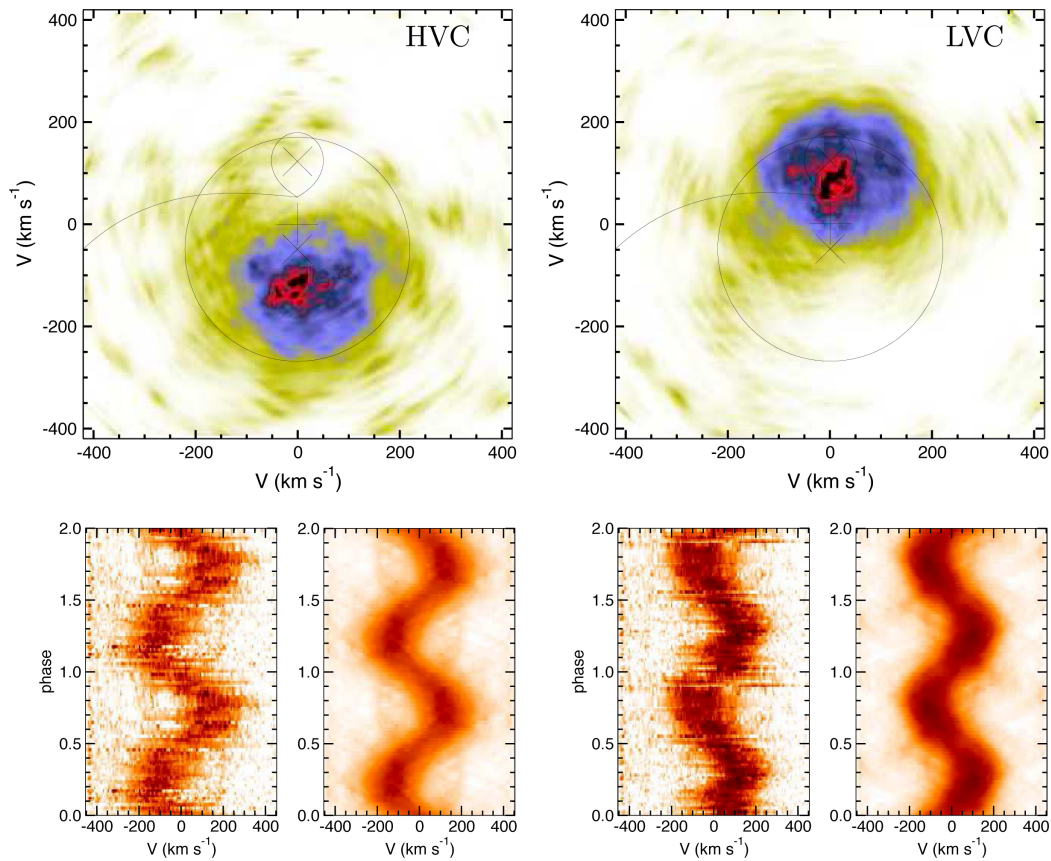
Figure 7. The trailed observed and reconstructed spectra of the H α components along with the Doppler maps are presented here. On the left-hand side the separated HVC trailed spectrum and its reconstruction are plotted at the bottom, while the corresponding velocity map of the HVC is displayed above. Respectively, on the upper right-hand side of the figure is the Doppler tomogram of the LVC with the separated observed and reconstructed trailed spectra at the bottom. The Keplerian velocity of the disc in the Doppler maps is located at $\upsilon_{disc} \sin(i) \geq 220$ km s^{-1} and the circle shows the disc's external radius. The system parameters are discussed in the text.

ballistic trajectory of the mass-transfer flow are overplotted, as well as a ring corresponding to the outer radius of the disc. To calculate them, we selected the mass of the WD, $M_{WD} = 0.8$ M$_\odot$, and the mass ratio, $q = 0.4$, as statistically average values for a $P_{orb} = 3.8$ h nova-like CV (Knigge, Baraffe & Patterson 2011; Zorotovic, Schreiber & Gänsicke 2011). The orbital inclination angle was fixed at $i = 25°$ (see Section 5 for justification of these parameters).

The LVC produces a spot converging with the position of the secondary in the velocity map. Apparently, this is a result of our phase allocation. Usually, when the irradiated secondary star forms the emission, the line is narrower (3.8 Å in the eclipsing RW Tri, Subebekova et al. 2020, against 5.3 Å in BG Tri), and the compact spot is concentrated in the hemisphere facing the WD. The reason for such a diffuse spot is not clear, but a low orbital inclination of the system probably contributes to it. Meanwhile, the HVC produces another diffuse and elongated concentration (top left), in a region that is clearly evading identification with either the stellar component of the binary, the accretion disc, or the mass-transfer stream, including the impact area of the stream with the disc. Detection of this H α component and its corresponding location in the velocity maps has become common for RW Sex-type NLs. Among a few possible explanations cited by Hernandez et al. (2017) and Subebekova et al. (2020), we prefer the model in which the outflow from the disc takes places in the orbital plane, instead of the wind perpendicular to the plane direction. Three-dimensional numerical simulations of the gas

dynamics show that such outflows are viable in the vicinity of the Lagrangian L3 point (Sytov et al. 2007). BG Tri provides a good argument in favour of this hypothesis: first, the object shows meagre emission from the He II line, even though we observe it almost face-on; hence it is difficult to argue that a disc wind is significant enough to produce an intense enough emission spectrum (e.g. Matthews et al. 2015) to overcome the bright accretion disc. Generally, P Cygni-like profiles for NLs are observed in UV and quite successfully modelled for recombination emission (Long & Knigge 2002), where the lines of low-inclination systems exhibit the characteristic imprint. However, reproducing this in the optical range is a challenging task; it produces some double-peaked emission line contribution only in high-inclination ($i > 60°$) systems. Matthews (2016) attempted to convert lines into single-peaked ones, requiring an extension of the line-forming region to $\sim$150 R_{WD}, which again works only for high inclinations. As a result, Matthews (2016) succeeded in producing a successful model for RW Tri by comparing it to a low-resolution spectrum of the object. But Subebekova et al. (2020) demonstrated that the H α in RW Tri is complex and at least partially formed at the heated surface of the secondary star. Secondly, H α emission has already been disentangled in four objects, including BG Tri, all of which have vastly different inclination angles. After correction for the inclination angle $i = 25°$ (see Section 5), the measured $\upsilon_{HVC}/\sin(i) = 121$ km s^{-1} of the HVC converts into 286 km s^{-1}. According to Hernandez et al. (2017) and Subebekova et al. (2020),
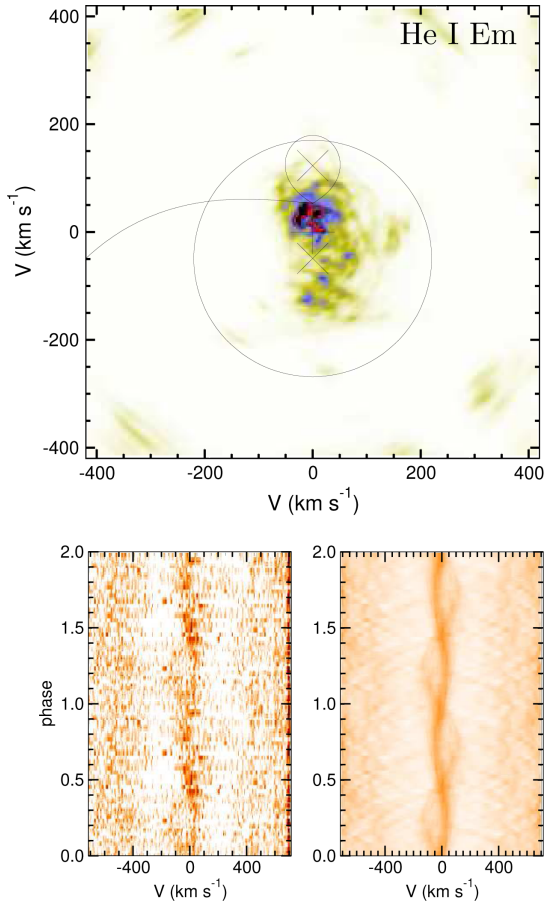

Figure 8. A Doppler map of He I λ5875.6 emission. The trailed spectrum and reconstructed trailed spectrum of the emission are presented at the bottom, the velocity map at the top. The Keplerian velocity of the disc in the Doppler maps is located at $\upsilon_{disc}\sin(i) \geq 220\,km\,s^{-1}$ and the circle shows the disc's external radius. The system parameters are discussed in the text.

the HVC (also called the 'wide component' in these publications) in all studied objects is $\approx 300\,km\,s^{-1}$, after the inclination angle has been accounted for. The fact that the HVC in all morphologically similar NL variables shows the same value after correction for a variety of inclination angles is good evidence that the source of the HVC is in the orbital plane. One would expect that the wind would constitute itself differently depending on the viewing aspect. Notwithstanding, the HVC always appears on the Doppler maps at the same spot, adjacent to the outer edge of the accretion disc on the opposite side to the secondary/hotspot, regardless of the system inclination.

Fig. 3 demonstrates that He I acts somewhat differently with respect to the Balmer lines. This is also a common characteristic of RW Sex-type NLs. Helium lines are fainter than Hα or Hβ ones and comprise equally intense emission and absorption. Nevertheless, we explored their phase evolution using illustrative trailed spectra and their respective tomograms. We concentrated on the He I λ 5875.6 line, which has the best S/N among helium lines. A trailed and reconstructed spectra of the emission component of this line and the corresponding tomogram are presented in Fig. 8. Meanwhile, the same line is treated as an absorption feature on the right-hand side. The emission component of the line basically repeats the pattern observed in Hα. The observed trailed spectrum is faint, but the program picks up the signal correctly, reflecting it in the reconstructed spectrum. The low-velocity component definitely

dominates, and hence a compact spot materializes close to the L1 point, in contrast with the diffuse appearance in the Hα case. The HVC is hardly traceable in the observed trailed spectra, but apparently some emission comes from here too. Hence, a coma-like extension in the velocity map is visible

5 SYSTEM PARAMETERS

The average mass of WDs in CVs above the period gap is $M_{WD}(P_{orb} > 3\,h) = 0.86(20)\,M_{\odot}$ (Zorotovic et al. 2011). For simplicity, we adopted $M_{WD} = 0.8\,M_{\odot}$. Taking into account the semi-empirical relation of secondary type versus orbital period, we expect a secondary with a mass of $M_2 \approx 0.3\,M_{\odot}$ and spectral type of M3V–M4V (Knigge 2006). The expected mass ratio and separations are $q \equiv M_2/M_{WD} \approx 0.4$ and $a = 1.23\,R_{\odot}$, respectively. The accretion-disc truncation radius[4] is $r_{disc}^{out} = 0.52\,R_{\odot}$. The corresponding primary, secondary, and L1 orbital velocities are 117, 292, and 129 km s^{-1}, respectively (see Fig. 9).

There are numerous flux measurements of BG Tri available in the public domain. We fetched all available data from VizieR[5] (Ochsenbein, Bauer & Marcout 2000). We revised the available data, since some measurements are erroneous (e.g. the SDSS data are not correct because the object is too bright), and compiled those that passed scrutiny in Table 2. Selected data are plotted using circles in the bottom panel of Fig. 10, after the interstellar reddening correction of $E(B - V) = 0.03$ (Green et al. 2015). Using the *Gaia* distance of $d = 334(8)$ pc, we can calculate the luminosity of different components. In particular, even a hot 50 kK white dwarf will have a negligible contribution to the optical flux. A secondary M3–4 V Roche lobe filling star has some insignificant influence in the IR. A comparison of the observed fluxes with those expected from different components confirms that the flux in the entire wavelength range is formed mostly by the accretion disc. The dashed lines in the bottom panel of Fig. 10 indicate a simple accretion-disc spectrum as a composition of multiple blackbodies, from concentric rings with a corresponding distribution of temperatures throughout the stationary optically thick disc (La Dous 1989). Since the observed flux would depend on the aspect of the disc, we fitted the observed SED as a function of the mass-transfer rate $\dot{M}$ and the system inclination.

The UV points were excluded from consideration because it is well known that accretion-disc models do not reproduce the observed spectrum shape of CVs in the wide range including the UV (Puebla, Diaz & Hubeny 2007).

For the fit's robustness, we added a spectrum of M3V-type stars from the empirical template library of the Sloan Digital Sky Survey stellar spectra (Kesseli et al. 2017), which was extended to the IR range using spectral templates from Rayner, Cushing & Vacca (2009). The star spectrum was scaled to the object's distance. For each band listed in Table 2 (except FUV and NUV) the flux m_{calc} was calculated as a sum of the disc model and the secondary. The result of the best fit of function $\chi^2 = \Sigma((m_{obs} - m_{calc})/\Delta m_{obs})^2$ is presented as a long-dashed line in the lower panel of Fig. 10. In the upper panel of Fig. 10, the goodness of fit is presented as an intensity scale diagram. Following the assumption that the LVC is emitted from the heated hemisphere of the companion star, the expected LVC velocity is located in the range of $\upsilon_{LVC} \in [130\sin(i), 290\sin(i)\,km\,s^{-1}]$ (see Fig. 9), which allows us to estimate limits on the orbit inclination from the dynamical constraints. The observed value of the LVC is

---

[4]Equation (2.61) from Warner (1995).
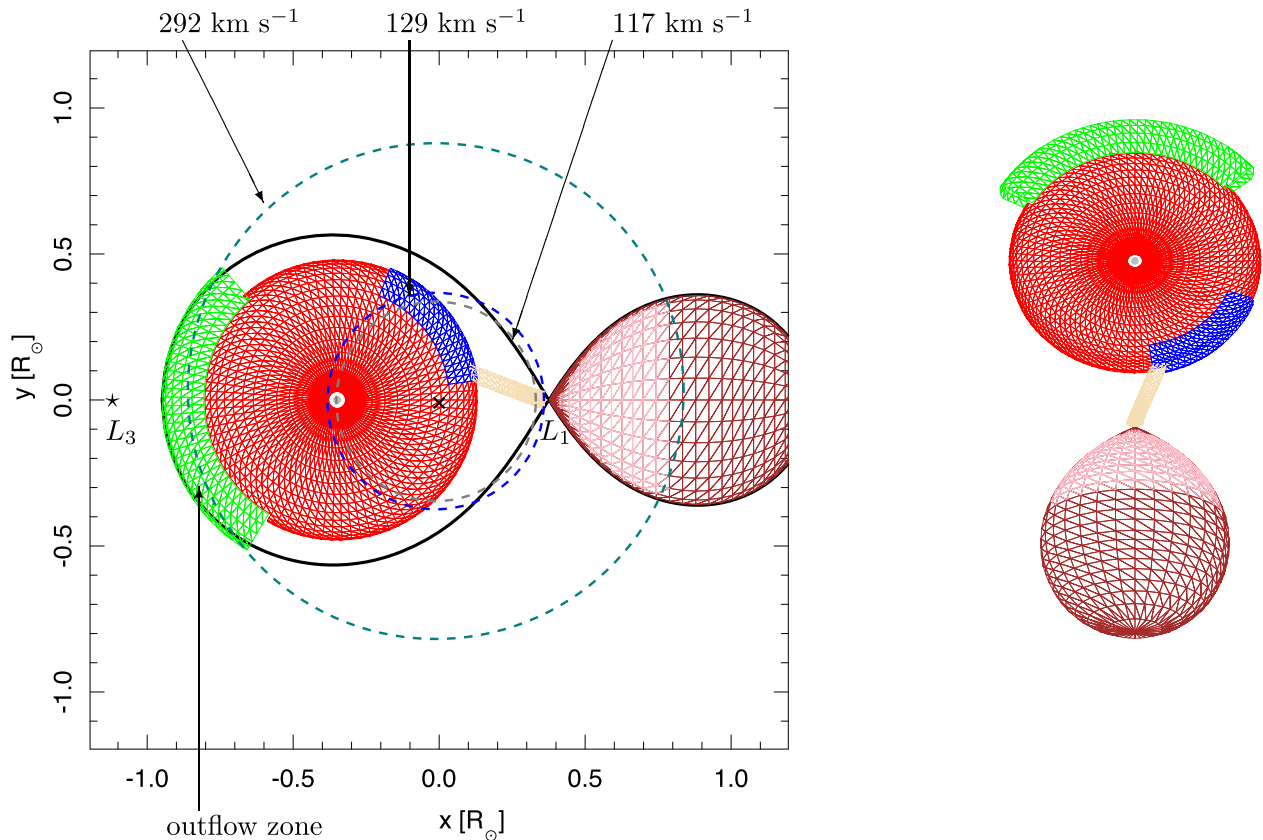[5]http://vizier.unistra.fr/vizier/sed/

Figure 9. A geometric model of BG Tri. The centre of mass (x) and corresponding Lagrangian points are marked. Velocities of the L1 point, the disc outflow area (green), and the WD are denoted. The LVC, which is emitted from the irradiated hemisphere of the secondary star, has a velocity exceeding that of the L1 point and less than the orbital velocity of the star.

$78 \, \mathrm{km \, s^{-1}}$, which defines the limits marked by the vertical dashed lines in Fig. 10, top. The line on the right-hand side of the plot indicates the observed LVC, which is consistent with the L1 point, and another corresponds to the centre of mass of the secondary (on the left-hand side). In other words, the inclination angle and mass accretion rate would be highest if the LVC is emitted just from the L1 point and, accordingly, lowest if the entire surface of the secondary is heated. Of course, neither assumption is correct, so we introduced some parameter that reflects the increasing cross-section of the secondary with decreasing temperature. According to this, the best fit is achieved at $i = 25(5)°$ and $\dot{M} = 8.0(1.0) \times 10^{-9} \, \mathrm{M_\odot \, yr^{-1}}$.

Given all uncertainties of adopted assumptions, the fit is remarkably good. The values of mass accretion rate are within the range of estimates for a number of other NLs (e.g. fig. 2 of Hameury 2019). The mass transfer $\dot{M}$ dependends slightly on the mass of the WD. For a $0.6 \, \mathrm{M_\odot}$ WD, the mass-transfer rate increases to $10^{-8} \, \mathrm{M_\odot \, yr^{-1}}$. On the downside, $\dot{M}$ is $\sim 4.0 \times 10^{-9} \, \mathrm{M_\odot \, yr^{-1}}$ for a massive $\geq 1.0 \, \mathrm{M_\odot}$ WD.

The LVC velocity corrected for a system inclination of $i = 25°$ is $\upsilon_{LVC} = 185 \, \mathrm{km \, s^{-1}}$. As we showed earlier, the corrected HVC velocity is $\approx 300 \, \mathrm{km \, s^{-1}}$, corresponding to the orbital velocity at the edge of the disc on the opposing side of the system relative to the secondary. The location of the HVC on Doppler maps of all similar NLs is related to the Lagrangian L3 point. According to some hydrodynamic models (Sytov et al. 2007; Lukin et al. 2017) an outflow of matter from the disc in to the orbital plane takes place

from this area (marked green in Fig. 9). The concentration of gas in that area might be responsible for the HVC or the wide component of emission lines in these objects.

6 CONCLUSIONS

We have studied BG Tri, one of the brightest CVs at $V = 11.9$, which has somehow escaped attention until now. We determined its orbital period to be $0.158 \, 45 \, \mathrm{d}$ or $3.8028 \, \mathrm{h}$. We show that it is an NL system, identified by its characteristic blue spectrum containing a set of H I and He I lines, comprising wide absorption features containing strong emission peaks. The orbital period and the spectrum, combined with the SED, indicate the presence of a bright accretion disc in a high density and temperature state, proper to NLs. The long-term light curve of BG Tri, obtained by ASAS SN and CRTS sky surveys, shows the absence of dwarf nova-style outbursts, but reveals an instance of low luminosity state often detected in NLs, also known as the VY Scl phenomenon.

Absorption lines originate from the optically thick accretion disc, while emission forms elsewhere. We demonstrate that the Balmer emission lines are complex and we are able to separate H α into two components. We identify the LVC with the heated surface of the secondary star facing the luminous disc. We associate the HVC with the disc outflow region situated on the opposite side of the disc to the secondary and the hotspot. A similar occurrence is also common for the NLs mentioned, which we may call RW Sex-type

Table 2. VizieR photometric data of BG Tri.

λ (μm)	Flux (× 10⁻³ Jy)	1σ flux × 10⁻³	Band	Source	Ref.
0.153	32.1	0.2	FUV	*GALEX*	1
0.231	19.3	0.1	NUV	*GALEX*	1
0.444	64.2	11.6	B	AAVSO	2
0.477	79.0		g	PAN-STARRS	3
0.482	64.6	9.3	g'	AAVSO	2
0.505	65.7	0.9	G_{BP}	*Gaia2*	4
0.554	61.4	9.6	V	AAVSO	2
0.613	63.2		r	PAN-STARRS	3
0.623	58.9	0.3	G	*Gaia2*	4
0.625	58.7	7.7	r'	AAVSO	2
0.748	51.6		i	PAN-STARRS	3
0.763	51.5	7.6	i'	AAVSO	2
0.772	49.6	0.7	G_{RP}	*Gaia2*	4
0.865	44.2		z	PAN-STARRS	3
0.960	36.5	0.8	y	PAN-STARRS	3
1.24	29.9	0.6	J	2MASS	5
1.65	20.6	0.4	H	2MASS	5
2.16	14.0	0.2	K_s	2MASS	5
3.35	6.85	0.15	W1	*WISE*	6
4.60	4.19	0.08	W2	*WISE*	6
1.16	0.89	0.09	W3	*WISE*	6

Notes. 1 – Bianchi, Shiao & Thilker (2017).
2 – Henden et al. (2015).
3 – Chambers et al. (2016).
4 – Gaia Collaboration et al. (2018).
5 – Cutri et al. (2003).
6 – Cutri et al. (2012).
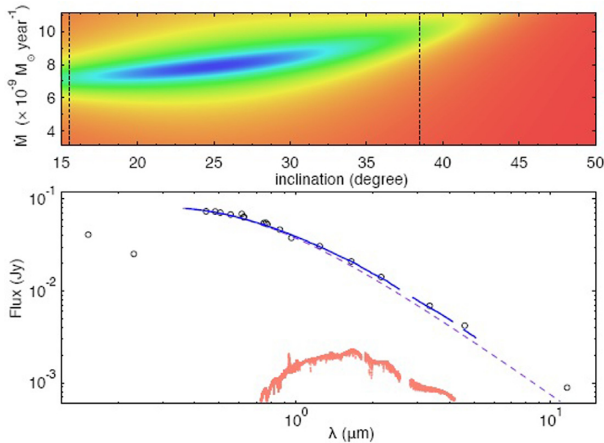
Figure 10. The plot of spectral energy distribution of BG Tri in the bottom panel. Circles represent the fluxes from Table 2. They were corrected for the interstellar extinction $E(B-V) = 0.03$. The dashed line through the observed data in the optical–IR range represents the spectrum of the accretion disc. The red points represent a spectrum of an M3V star scaled to a 337 pc distance. The solid line is a combination of fluxes from the accretion disc and the secondary. The outermost two points on the left correspond to UV data. In the upper panel the best-fitting parameters (mass accretion rate versus inclination angle) of the accretion-disc model to the data are presented in the form of an intensity map. The extreme boundaries of i corresponding to the secondary mass centre and L1 point are marked by vertical lines. The preferred values of $\dot{M}$ and i (blue strip) are also a function of increasing surface and decreasing temperature along the latitude.

systems, all of which are concentrated in a 3–6 h range of orbital periods (Subebekova et al. 2020). An HVC velocity, corrected for the inclination angle of ∼300 km s⁻¹, is very definite in all studied objects, regardless of their orientation. That, in our opinion, argues against the disc-wind origin of the HVC component. However, it is not evidence of the absence of wind, just a rationalization that emission lines in the optical range are not formed in the wind.

The SED of BG Tri confirms that the stellar-component contribution is negligible and that most of the flux from the UV to the near-IR is emitted by the disc. The energy balance supports the idea that we observe the system nearly face-on, and the deduced inclination angle validates the value obtained from the dynamical considerations.

DATA AVAILABILITY

The data underlying this article will be shared on reasonable request to the corresponding author.

REFERENCES

Abril J., Schmidtobreick L., Ederoclite A. r., López-Sanjuan C., 2020, MNRAS, 492, L40
Bailer-Jones C. A. L., Rybizki J., Fouesneau M., Mantelet G., Andrae R., 2018, AJ, 156, 58
Baptista R., Steiner J. E., Horne K., 1996, MNRAS, 282, 99
Beuermann K., Stasiewski U., Schwope A. D., 1992, A&A, 256, 433
Bianchi L., Shiao B., Thilker D., 2017, ApJS, 230, 24
Chambers K. C. et al., 2016, preprint (arXiv:1612.05560)
Cutri R. M., Skrutskie M. F., van Dyk S., 2003, 2MASS All Sky Catalog of point sources
Cutri R. M. et al., 2012, VizieR Online Data Catalog: WISE All-Sky Data Release (Cutri+ 2012)}, II/311
Dhillon V. S., Smith D. A., Marsh T. R., 2013, MNRAS, 428, 3559
Drake A. J. et al., 2009, ApJ, 696, 870
Gaia Collaboration et al., 2018, A&A, 616, A1
Green G. M. et al., 2015, ApJ, 810, 25
Guerrero M. A. et al., 2018, ApJ, 857, 80
Hameury J.-M., 2020, Advances in Space Research, 66, 5
Hellier C., 1996, ApJ, 471, 949
Henden A. A., Levine S., Terrell D., Welch D. L., 2015, in American Astronomical Society Meeting Abstracts, Vol. 225, p. 336.16

Hernandez M. S., Zharikov S., Neustroev V., Tovmassian G., 2017, MNRAS, 470, 1960

Hernández Santisteban J. V., Echevarría J., Michel R., Costero R., 2017, MNRAS, 464, 104

Hewitt D. M. et al., 2020, MNRAS, 496, 2542

Horne K., 1986, PASP, 98, 609

Howell S. B., Mason E., 2018, AJ, 156, 198

Kesseli A. Y., West A. A., Veyette M., Harrison B., Feldman D., Bochanski J. J., 2017, ApJS, 230, 16

Khruslov A. V., 2008, Peremennye Zvezdy Prilozhenie, 8, 4

King A. R., Cannizzo J. K., 1998, ApJ, 499, 348

Knigge C., 2006, MNRAS, 373, 484

Knigge C., Baraffe I., Patterson J., 2011, ApJS, 194, 28

Kochanek C. S. et al., 2017, PASP, 129, 104502

Kolb U., King A. R., Ritter H., 1998, MNRAS, 298, L29

La Dous C., 1989, A&A, 211, 131

Lasota J.-P., 2001, New Astron. Rev., 45, 449

Lenz P., Breger M., 2005, Communications in Asteroseismology, 146, 53

Lenz P., Breger M., 2014, Period04: Statistical analysis of large astronomical time series, preprint (ascl:1407.009)

Levine S., Chakarabarty D., 1995, IA-UNAM Technical Report MU-94-04

Livio M., Pringle J. E., 1994, ApJ, 427, 956

Long K. S., Knigge C., 2002, ApJ, 579, 725

Lukin V. V., Malanchev K. L., Shakura N. I., Postnov K. A., Chechetkin V. M., Utrobin V. P., 2017, MNRAS, 467, 2934

Makarov V. V., 2017, Rev. Mex. Astron. Astrofis., 53, 439

Marsh T. R., 2005, Ap&SS, 296, 403

Marsh T. R., Horne K., 1988, MNRAS, 235, 269

Martin C. et al., 2003, in Blades J. C., Siegmund O. H. W., eds, SPIE Conf. Ser. Vol. 4854, Future EUV/UV and Visible Space Astrophysics Missions and Instrumentation, p. 336

Matthews J. H., 2016, PhD thesis, Univ. Southampton

Matthews J. H., Knigge C., Long K. S., Sim S. A., Higginbottom N., 2015, MNRAS, 450, 3331

Murray N., Chiang J., 1996, Nature, 382, 789

Ochsenbein F., Bauer P., Marcout J., 2000, A&AS, 143, 23

Patterson J., Patino R., Thorstensen J. R., Harvey D., Skillman D. R., Ringwald F. A., 1996, AJ, 111, 2422

Puebla R. E., Diaz M. P., Hubeny I., 2007, AJ, 134, 1923

Rappaport S., Verbunt F., Joss P. C., 1983, ApJ, 275, 713

Rayner J. T., Cushing M. C., Vacca W. D., 2009, ApJS, 185, 289

Ritter H., Kolb U., 2003, A&A, 404, 301

Ritter H., Kolb U., 2003b, A&A, 404, 301

Rodríguez-Gil P. et al., 2007, MNRAS, 377, 1747

Rodríguez-Gil P. et al., 2015, MNRAS, 452, 146

Rodríguez-Gil P. et al., 2020, MNRAS, 494, 425

Rodríguez-Gil P., Schmidtobreick L., Gänsicke B. T., 2007a, MNRAS, 374, 1359

Rodríguez-Gil P. et al., 2007b, MNRAS, 377, 1747

Schmidtobreick L., Mason E., Howell S. B., Long K. S., Pala A. F., Points S., Walter F. M., 2018, A&A, 617, A16

Shafter A. W., 1992, ApJ, 394, 268

Shafter A. W., Wheeler J. C., Cannizzo J. K., 1986, ApJ, 305, 261

Shappee B. J. et al., 2014, ApJ, 788, 48

Spruit H. C., 1998, preprint (astro-ph/9806141)

Subebekova G., Zharikov S., Tovmassian G., Neustroev V., Wolf M., Hernandez M. S., Kučáková H., Khokhlov S., 2020, MNRAS, 497, 1475

Sytov A. Y., Kaigorodov P. V., Bisikalo D. V., Kuznetsov O. A., Boyarchuk A. A., 2007, Astron. Rep., 51, 836

Thorstensen J. R., Ringwald F. A., Wade R. A., Schmidt G. D., Norsworthy J. E., 1991, AJ, 102, 272

Tovmassian G., Stephania Hernandez M., González-Buitrago D., Zharikov S., García-Díaz M. T., 2014, AJ, 147, 68

Tovmassian G., González J. F., Hernández M. S., González-Buitrago D., Zharikov S., Hernández Santisteban J. V., 2018, ApJ, 869, 22

Townsley D. M., Gänsicke B. T., 2009, ApJ, 693, 1007

Vorontsov-Velyaminov B., 1934, The Observatory, 57, 157

Warner B., 1976, in Eggleton P.ed., Proc. IAU Symp. 73, p. 85

Warner B., 1986, MNRAS, 222, 11

Warner B., 1987, MNRAS, 227, 23

Warner B., 1995, Cambridge Astrophysics Series, 28

Warner B., van Citters G. W., 1974, The Observatory, 94, 116

Woźniak P. R. et al., 2004, AJ, 127, 2436

Zorotovic M., Schreiber M. R., Gänsicke B. T., 2011, A&A, 536, A42

Zorotovic M. et al., 2016, MNRAS, 457, 3867

This paper has been typeset from a TeX/LaTeX file prepared by the author.